International Journal of Heat and Mass Transfer 168 (2021) 120837

Contents lists available at ScienceDirect

International Journal of Heat and Mass Transfer

journal homepage: www.elsevier.com/locate/hmt

Simulation of melt film dynamics in laser fusion cutting using a boundary layer approximation

U. Halm [a,*], M. Nießen [b], W. Schulz [a,b]

[a] Nonlinear Dynamics of Laser Processing, RWTH Aachen University, Steinbachstr. 15, Aachen 52074, Germany
[b] Fraunhofer Institute for Laser Technology, Steinbachstr. 15, Aachen 52074, Germany

ARTICLE INFO

Article history:
Received 14 September 2020
Revised 14 December 2020
Accepted 15 December 2020

Keywords:
Laser fusion cutting
Computational fluid dynamics
Boundary layer approximation

ABSTRACT

Process inherent instabilities in the dynamics of the thin melt film during laser fusion cutting reduce the quality of the cut surface with regards to mean profile height and angular tolerance. To enhance the process understanding and to identify and evaluate quality improvement measures, a 3*D* model of the melt film dynamics is developed and applied to experimental results from literature. To cope with the multi-scale character of the mathematical task, model reduction techniques are applied: the underlying transport equations are mapped to a conformal coordinate system and subjected to a scaling analysis. By using a perturbation series, the most significant contributions to the equations of motion are selected. An integral boundary layer approximation reduces the dimension of the numerical task to a two-dimensional problem that can be solved with very low computational effort. The resulting simulation is able to reflect the dynamics at a spatial resolution below $\Delta x \leq 25\,\mu$m and a temporal resolution below $\Delta t \leq 2.5\,\mu$s within a reasonable calculation time of a few days for a cut length of $L = 10$ mm and a cut thickness of $a = 3$ mm. Known correlations between process parameters and quality features are reproduced by this simulation. Results show that a concurrent improvement of mean profile height and angular tolerance cannot be obtained by straightforward measures like changing the beam profile from tophat to Gaussian and vice-versa. Future work will be focused on the extension of this model with regards to surface tension and evaporation.

1. Introduction

During oxygen-free laser fusion cutting of sheet metal, process inherent instabilities in the dynamics of the thin melt film cause irregular solidification patterns on the cut surface, so-called striations characteristic of this process (Fig. 1). Along with the angular tolerance (Fig. 2) of the cut surface and a minimum adherence of dross at the lower cut edge, the mean profile height of the cut surface represent the most important quality features in laser cutting.

The characteristics of the striation pattern depend significantly on the laser source selected, the shape of the laser beam, the cutting speed, the laser power and the assist gas flow. Due to the propagation and absorption characteristics of the generated laser light, modern low-cost and energy-efficient solid-state laser sources show an inferior cut quality compared to energy-intensive CO_2 laser systems. An enhanced understanding of the correlation between absorption and the emergence of melt waves can point out new measures to improve the quality.

In the presented paper a numerical model is derived that will be able to reflect essential properties of the dynamics of the melt film and to evaluate the impact of various compensation strategies on the quality of the cut. For this purpose

- dominant scales and sub-processes are identified.
- the corresponding mathematical task is reduced by a perturbation series so that a highly resolved simulation provides statements on relevant quality features within a reasonable computation time.
- dependencies between process parameters and quality features are analyzed to derive measures to improve the quality of the cut.

The analysis points to a significant influence of the beam shape. Besides the wavelength of the laser light, solid-state and CO_2 laser systems today usually operate with different beam shapes. CO_2 system commonly provide a nearly Gaussian beam shape [2] while solid-state lasers operate with tophat-like shapes [3]. This difference is partially due to beam generation and guiding but also

* Corresponding author.:.
E-mail address: ulrich.halm@nld.rwth-aachen.de (U. Halm).

https://doi.org/10.1016/j.ijheatmasstransfer.2020.120837

Nomenclature

w	Cut surface profile
a	Cut thickness
x'	Global coordinate, cutting direction
y'	Global coordinate, lateral direction
z'	Global coordinate, neg. beam direction
z	Conformal coordinate, axial direction
U	Angular tolerance or perpendicularity
Δa	Thickness reduction
R_{z5}	Mean profile height
R_a	Average surface roughness
L	Cut length
P_L	Laser power
v_0	Cutting speed
z_0	Focal point
z_R	Rayleigh length
w_0	Laser beam radius
λ	Laser wavelength
M^2	Laser beam quality factor
v_g	Velocity of assist gas flow
v_m	Typical magnitude of melt velocity
t_m	Typical melt film thickness
$\mathbf{v}$	Unscaled velocity
t	Unscaled time
ϱ	Mass density
p	Unscaled pressure
T	Unscaled temperature
κ	Thermal diffusivity
Γ_*^m	Melt boundary
$\Omega_{[s,l]}$	Solid, liquid volume
Q_s	Unscaled heat flux into solid
Q_l	Unscaled heat flux into liquid
Q_a	Unscaled absorbed heat flux
h_m	Specific heat of fusion
v_p	Unscaled velocity of phase boundary
v_p^a	Unscaled velocity of absoption boundary
$\mathbf{v}_{in}$	Unscaled inflow velocity into liquid phase
T_m	Melting temperature
$\mathfrak{S}$	Stress tensor
p_g	Unscaled assist gas pressure
σ	Surface tension
$\mathcal{K}$	Curvature
$\mathbf{t}_{[1,2]}$	Surface tangential
$\tau_{g[1,2]}$	Unscaled driving forces
$\tau_{[\alpha,z]}$	Scaled driving forces
H	Unscaled melt film thickness
h	Scaled melt film thickness
α	Conformal coordinate, azimuthal direction
ν	Conformal coordinate, neg. radial direction
$h_{[\nu,\alpha,z]}$	Scaling factors for conformal coordinate system
τ	Scaled time
$\mathbf{u}$	Scaled velocity (u_ν, u_α, u_z)
θ	Scaled temperature
ν_l	Kinematic viscosity
T_a	Ambient temperature
Π	Scaled pressure
γ	Small parameter
δ	Small parameter
ϵ	Small parameter
Re	Reynolds number
Re^*	Scaled Reynolds number $\epsilon\mathrm{Re}$
$\mathbf{u}_m$	Scaled inflow $(u_{m\nu}, u_{m\alpha}, u_{mz})$
m_α	Integrated mass flux azimuthal direction
m_z	Integrated mass flux axial direction
Π_g	Scaled assist gas pressure
$h_{\min}$	Minimum melt film thickness
q_a	Scaled absorbed energy flux density
μ	Cosine of angle of incidence
$\hat{\mathbf{S}}$	Direction of incidence of laser light
$A_{[s,p]}$	Absorption coefficient perpendicular, parallel
ϵ_λ	Absorption parameter for wavelength λ
Φ	Phase factor for laser light
q_l	Scaled heat flux into liquid
q_s	Scaled heat flux into solid
ϕ	Distance function for phase boundary
c_p	Specific heat capacity
k	Heat conductivity
H_m	Heat of fusion
λ_R	Striation wavelength

result of an optimization for two quality features: mean profile height and angular tolerance.

1.1. Research questions

To deepen the understanding for this difference, two research questions are formulated and analyzed:

(1) How does the slope of the beam profile affect the qualify features angular tolerance and mean profile height?
(2) Can the difference in quality between solid-state and CO_2 laser systems partially be explained by different beam profiles and how should a beam profile for solid-state lasers look like to produce a nearly perpendicular cut surface with a minimal slope of the beam profile?

1.2. Technical motivation

According to the norm EN ISO 9013 [1] essential quality features of thermal cuts are perpendicularity or angular tolerance and mean profile height. The mean profile height R_{z5} is defined by the arithmetic mean of the difference of the maximum values w_n^+ and minimum values w_n^- of five bordering single measurement distances Eq. (1) at a total measurement distance $L = 15\,\mathrm{mm}$. Another measure often used in literature is the average surface roughness R_a as integrated deviation of the profile height w from the mean profile height $\bar{w}$.

$$R_{z5} = \frac{1}{5}\sum_{n=1}^{5} w_n^+ - w_n^- \tag{1}$$

$$R_a = \frac{1}{L}\int_0^L |w - \bar{w}|\,dx' \tag{2}$$

The angular tolerance U is defined as the difference of maximum and minimum values of the surface profile at a constant position x' along the cut. To avoid errors due to rounding at top and dross formation at bottom, the topmost and lowermost 10% of the cut surface are not taken into account (Fig. 2).

The technical motivation accounted in this paper is to reduce the measures R_{z5} and U to improve the quality of the cut. The R_{z5} measure is calculated at 75% cut depth using a measurement distance of $L = 5\,\mathrm{mm}$. The mean angular tolerance $\bar{U}$ is calculated as arithmetic mean within this measurement distance (Fig. 3).

The process parameters are given in Tab. 1. *Reference I* refers to usual cutting parameters used in technical applications. These parameters are used for later scaling analysis required for the derivation of the reduced model. The simulation developed is not yet

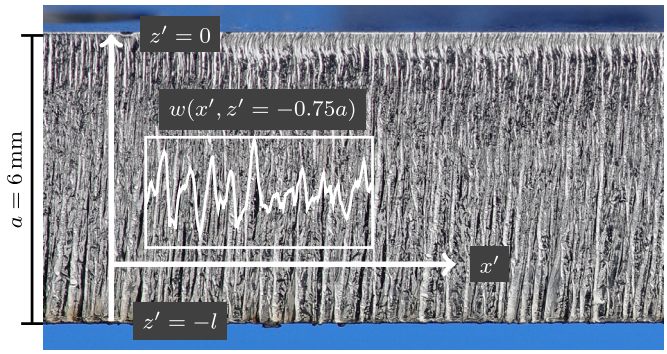

Fig. 1. Cut surface in laser fusion cutting of stainless steel with thickness $a = 6\,\mathrm{mm}$. The surface profile $w(x, z)$ shows a certain roughness due to instabilities in the melt film during cutting.

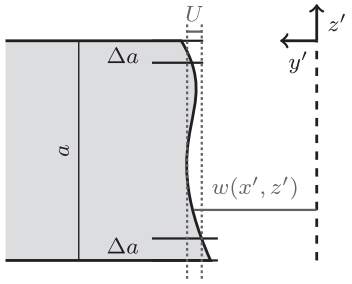

Fig. 2. Measurement of angular tolerance U referring to EN ISO9013 [1]. The half width of the kerf $w(x, z)$ describes the cut surface. The thickness reduction Δa is usually 10% of the cut thickness.

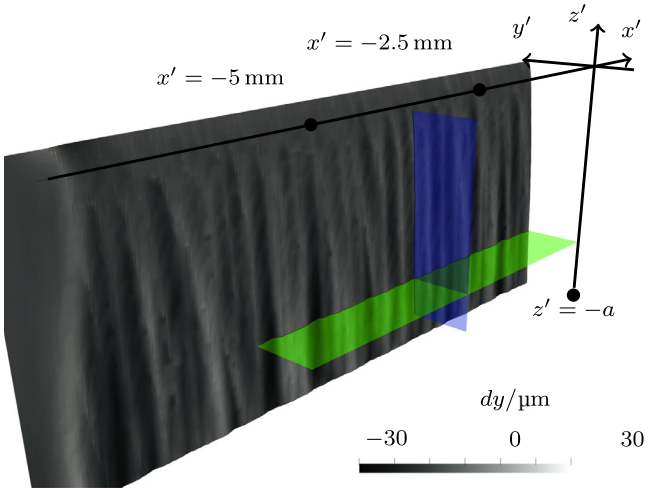

Fig. 3. Simulated surface profile for laser cuts and measurement planes for mean profile height R_{z5} at 75% depth (green) and angular tolerance U (blue). (For interpretation of the references to colour in this figure legend, the reader is referred to the web version of this article.)

stable enough to calculate quality features for this reference point. Evaluations within this paper are carried out with the parameters given as *Reference II* and are taken from Hirano [4]. This parameter set is optimized for experimental observation and is characterized by a large focus diameter, large laser power and low assist gas pressure. The resulting relatively calm melt film dynamics is well suited for simulative study.

Table 1
Process parameters used for this paper. *Reference I* indicates the parameters used for the scaling analysis to derive the model. *Reference II* indicates the parameters used by Hirano [4]. Parameter set *II* is used for the numerical investigations in this paper. The US name for EN 1.4301 steel grade is AISI 304.

Parameter	Symb./Unit	Ref. *I*	Ref. *II*
Material		1.4301	1.4301
Cut thickness	a/mm	6	3
Laser power	P_L/kW	4	8
Cutting speed	v_0/m min^{-1}	2.5	1
Focal point	z_0/mm	0	0
Rayleigh length	z_R/mm	5	30
Beam radius	w_0/μm	300	850
Wavelength	λ/μm	1	1
Assist gas pressure	p_g/bar	20	2.5

1.3. Related work

Stelzer et al. [5] compared mean profile heights in sheet metal cutting of stainless steel for a cut thickness $a = 10\,\mathrm{mm}$ using CO_2 and fiber lasers with a comparable Rayleigh length. For the CO_2 laser a mean profile height of $R_{z5} = 30\,\mu\mathrm{m}$ has been achieved and for the fiber laser $R_{z5} = 80\,\mu\mathrm{m}$. Noticeable is that the measured beam quality factor $M^2 = 1.6$ for the CO_2 system is significantly smaller than for the fiber system $M^2 = 6.2$. This supports the research question (2) given in the introduction that current fiber and CO_2 laser systems are operating with differing beam shapes.

Hirano and Fabbro [4] observed a stabilization of the melt film surface with increasing cutting speed using a disc laser. The parameters are given as *Ref. II* in Tab. 1 and are used for the studies in this paper. For a small cutting speed of $v_0 = 1\,\mathrm{m\,min^{-1}}$ the existence of melt humps that slide down the central part of the kerf has been confirmed. The processes on the side of the kerf are decoupled from the melt film dynamics near the apex of the cutting front. By increasing the cutting speed, the cutting front becomes more tilted and a stabilization of the melt film dynamics has been observed. The known correlation between increased cutting speed and reduced mean profile height could be approved. By linear stability analysis Hirano and Fabbro [6] explained that instabilities in the melt film that occur on the side of the kerf or that are transported from the center to the side are excited considerably lower for CO_2 lasers compared to solid-state lasers. Amara et al. [7] analyzed these results using the commercial FLUENT solver and reproduced the findings of Hirano and Fabbro for small cutting speeds. By adjusting the absorption properties for CO_2 laser radiation they observed a decreased inclination of the cut surface.

Arntz et al. [8] used trim cut diagnosis to show the effect of multiple reflections on the cut surface. For a cut thickness of $a = 6\,\mathrm{mm}$ a remelting of the cut surface in the lower third of the cut has been approved. Zaitsev et al. [9] analyzed the appearance of multiple reflections on the cut surface using a one-phase model that only considers the solid phase and assumes instant and ideal removal of the melt. For fiber lasers a significant effect of multiple reflections was already found for cut thicknesses $a \geq 1.5\,\mathrm{mm}$.

Otto and Schmidt [10] presented a numerical simulation environment based on the finite volume solver OPENFOAM. The application of this solver to a laser cutting task with a cut thickness of $a = 1\,\mathrm{mm}$ for CO_2 laser radiation reproduced typical quality losses [11].

Zhao and Peng [12] use a lattice Boltzmann based approach to perform a 3*D* simulation of sheet metal cutting. For cut thicknesses up to $a \leq 1\,\mathrm{mm}$ known relations between severance energy and cut thickness can be reproduced. Variation of assist gas velocity $250\,\mathrm{m\,s^{-1}} \leq v_g \leq 1000\,\mathrm{m\,s^{-1}}$ shows a minor effect on critical cut-

ting speed – laser power relations for $a = 0.6\,\mathrm{mm}$. Therefore assist gas pressure and shear force distribution is assumed constant in time in the work presented.

1.4. Preliminaries

The essential characterization of time scales of the motion of the free moving interface solid-gaseous in two dimensions neglecting the liquid phase has been presented by Schulz et al. [13]. Based on an approximation with integral dynamical variables at the apex of the cutting front, the generation of striations could be modeled as non-linear response to external perturbations [14].

Vossen and Schüttler [15] demonstrated a linear stability analysis at the apex of the cutting front. The implemented model can be used to analyze measures to prevent perturbations in the melt film from growing. One main finding is that a standard solid-state laser setup tends to excite perturbations up to significant melt waves, while a CO_2 setup is able to damp external perturbations and retain a stable melt film at the apex.

The complete three-dimensional mathematical task for modeling of laser fusion cutting has been given by Schulz et al. [16]. Jansen et al. [17] presented the basic concept used in this paper. The combination of several model reduction techniques and assumptions enables the development of a three-dimensional model of the melt film dynamics in laser fusion cutting. The results of the fully implemented model are presented in this paper.

1.5. Conclusion of related work and preliminaries

3*D* modeling of melt film dynamics is a demanding challenge, whose difficulty lies mainly in the multi-scale character of the underlying task and two coupled freely moving interfaces: solid-liquid and liquid-gaseous. Velocities in the melt up to and greater than $v_m \gtrapprox 10\,\mathrm{m\,s^{-1}}$ and melt film thicknesses around $t_m \approx 10\,\mu\mathrm{m}$ lead to temporal scales in the micro-second regime. The dimensions of the task with cut thicknesses greater than $a \geq 1\,\mathrm{mm}$, cut lengths around $L \approx 5\,\mathrm{mm}$ and striation frequencies at several hundreds of micrometers demand a numerical resolution below $\Delta x \lessapprox 100\,\mu\mathrm{m}$ in space and $\Delta t \lessapprox 10\,\mu\mathrm{s}$ in time. Without proper mathematical, physical and phenomenological reduction techniques, the resulting 3*D* simulation would create a computational effort that could not be solved within a reasonable time frame and the hardware available today.

2. Methodology

The aim of this work is to enable a fast simulation of melt film dynamics during laser fusion cutting and to enable a qualitative prediction of the tendency of the process to form pronounced striations or non-perpendicular cut surfaces. For this purpose elaborate model reduction techniques are used to reduce the complexity of the numerical task to a manageable level. The presented model

- reflects the melt film dynamics at the apex of the cutting front and its effect on the processes on the cut surface.
- takes beam shape, beam propagation and absorption into account.
- analyzes the dynamics of the melting front, neglecting complex phenomena like adherent dross and feedback effects from the assist gas flow.
- considers material properties as constant.
- allows a quantitative study of the quality features angular tolerance and mean profile height.
- is capable to display current compensation strategies like spatiotemporal modulation of the beam and closed loop control approaches.

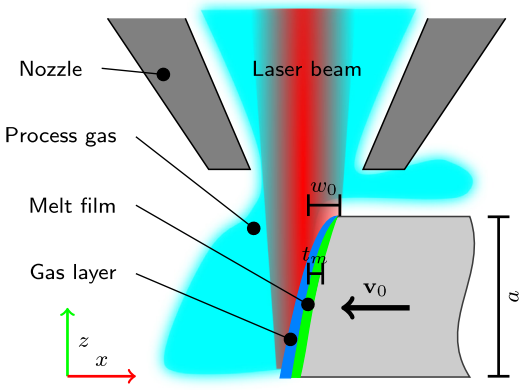

Fig. 4. 2*D* sketch of laser fusion cutting including length scales.

- enables the highly resolved simulation of the melt film dynamics within a reasonable calculation time and thus extended parameter studies.

Therefor the temperature in the solid phase is calculated numerically by a standard finite element approach. Using an integral method and a quadratic ansatz for the velocity field inside the melt film on a conformal coordinate system, a mathematically reduced description is retrieved.

Schulz et al. identified a hierarchy of spatial dimensions that is depicted in Fig. 4 for a typical sheet metal cutting task. The scale of the axial $z-$direction is the cut thickness a, which is much greater than the lateral length scale of the laser beam w_0, which is again much greater than the radial length scale of the melt film t_m. It follows

$$t_m \ll w_0 \ll a\,. \tag{3}$$

The presence of this hierarchy of spatial dimension in the conformal description of the melt film allows the expansion of the underlying equations of motions into a perturbation series. The power series solution [18] of the dynamic quantities velocity, pressure and temperature enables a hierarchical solution sequence with high accuracy at critical and reduced accuracy at smooth regions of the melt film.

2.1. Mathematical task

The mathematical task of laser fusion cutting is presented by Schulz et al. [16]. Details about the absorbed heat flux are given by Mahrle and Beyer [19]. The Navier-Stokes equations to describe the melt film dynamics include the balance of mass, the Cauchy momentum equation in conservative form neglecting the gravitational force and the heat flux equation as energy balance

$$\begin{aligned} \nabla\cdot\mathbf{v} &= 0 && \text{Mass}\,,\\ \frac{\partial\mathbf{v}}{\partial t} + (\mathbf{v}\cdot\nabla)\mathbf{v} &= -\frac{1}{\varrho}\nabla p + \nu_l\Delta\mathbf{v} && \text{Momentum},\\ \frac{\partial T}{\partial t} + (\mathbf{v}\cdot\nabla T) &= \kappa\,\Delta T && \text{Energy}\,, \end{aligned} \tag{4}$$

for the quantities flow velocity $\mathbf{v} = \mathbf{v}(\mathbf{x}, t)$, temperature $T = T(\mathbf{x}, t)$ and pressure $p = p(\mathbf{x}, t)$ for $\mathbf{x} \in \Omega_l(t)$ and the material parameters mass density ϱ, kinematic viscosity ν_l and thermal diffusivity $\kappa = k/\varrho c_p$. The liquid domain Ω_l is bound by the absorption boundary Γ_a^m on top of the melt facing the laser beam, the outflow boundary Γ_o^m on the bottom side of the sheet, the inflow boundary Γ_i^m between the solid and the liquid phase, the symmetry boundary Γ_s^m in the $y = 0$ plane and two virtual boundaries on top Γ_t^m

and at the backside of the melt Γ_b^m that should have zero radial extent (Fig. 5 and Fig. 6)

For a given heat flux $Q_{[s,l]} = k\nabla T_{[s,l]} \cdot \mathbf{n}$ for the solid and the liquid phase, an inflow $\mathbf{v}_{in}$ and a fixed temperature at melting temperature T_m, the boundary conditions for the melting boundary Γ_m are given as

$$Q_s = Q_l - \varrho h_m v_p,\ T = T_m,\ \mathbf{v} = \mathbf{v}_{in},\ \mathbf{x} \in \Gamma_i^m\ . \tag{5}$$

with specific melting enthalpy h_m and normal velocity of the phase boundary v_p.

At the absorption boundary Γ_a^m no material is transferred in normal direction $\mathbf{n}$ and the normal velocity of the phase boundary is v_p^a. The assist gas pressure p_g and the Laplace pressure for the surface tension σ and the curvature $\mathcal{K}$ act as load for the normal component of the stress tensor, the driving forces $\tau_{g[1,2]}$ and the thermal gradient of the surface tension act as load for the tangential components in the tangential directions $\mathbf{t}_{[1,2]}$. The absorbed energy flux density Q_a of the laser beam acts as load for the temperature T.

$$\begin{aligned} \varrho(\mathbf{v} - v_p^a\mathbf{n})\mathbf{n} &= 0\ , \\ \mathbf{n}(\mathfrak{S}\mathbf{n}) &= -p_g + \sigma\mathcal{K}\ , \\ \mathbf{t}_{[1,2]}(\mathfrak{S}\mathbf{n}) &= \tau_{g[1,2]} - \tfrac{\mathrm{d}\sigma}{\mathrm{d}T}\left(\nabla T \cdot \mathbf{t}_{[1,2]}\right)\ , \\ k\nabla T \cdot \mathbf{n} &= Q_a \end{aligned} \tag{6}$$

for $\mathbf{x} \in \Gamma_a^m$ and the thermal conductivity k. The stress tensor $\mathfrak{S}$ for incompressible fluids is the sum of a hydrostatic and a viscous contribution

$$\mathfrak{S} = -p\mathfrak{I} + \eta\left(\nabla \otimes \mathbf{v} + (\nabla \otimes \mathbf{v})^T\right) \tag{7}$$

with the identity $\mathfrak{I}$, the dynamic viscosity η and the dyad $\mathbf{a} \otimes \mathbf{b} = \mathbf{a}\mathbf{b}^T$.

At the bottom boundary Γ_b^m, a continuity boundary condition is applied to describe the outflow of the molten material. Formation of adherent dross is neglected in this stage of the model.

The melt film thickness H is described by a kinematic boundary condition. The surface of the melt film is given by the implicit function

$$H(\mathbf{x}, t) = 0, \quad \mathbf{n} = \nabla H, \quad \mathbf{x} \in \Gamma_a(t)\ . \tag{8}$$

By neglecting the evaporation mass flux, the normal velocity of the surface H equals the normal velocity of the melt. Using the incompressibility $\nabla \cdot \mathbf{v} = 0$ the evolution of the melt film thickness is given by

$$\partial_t H + \mathbf{v} \cdot \nabla H = 0 \tag{9}$$

An initial distribution $H(\mathbf{x}, t = 0) = H_0(\mathbf{x})$ is set for the kinematic boundary condition. At the top and backward boundaries H is set to zero.

2.2. Coordinate system for the solid phase

A Cartesian coordinate system is selected for the solid phase. Its origin is placed at the intersection point of the laser beam axis and the top surface of the sheet, shifted by an offset x_{off} into negative $x-$direction. The offset x_{off} is in the order of magnitude of the laser beam radius w_0 and necessary for the motion of the Lagrangian mesh that is used in the simulation. The structured hexahedral mesh is aligned along radial rays and the solid-liquid boundary is moved along these rays. Behind the radial part of the mesh, a rectangular mesh is attached for the thermal calculation. The motion of the rear edge of the surface of the radial region (Γ_b^m) is recorded to provide a highly resolved reconstruction of the cut surface profile.

2.3. Coordinate system for the liquid phase

The conformal coordinate system for the liquid phase is a specialization of a cylindrical coordinate system. We describe the surface of the melting front $\mathbf{x}_m$ as function of the azimuthal coordinate α and the axial coordinate z. The radial coordinate inside the melt film is called ν. With the distance the of melting front to the $z-$axis r_m, we can express $\mathbf{x}_m$ as

$$\mathbf{x}_m(\alpha, z, t) = \mathbf{x}_0(t) + z\hat{\mathbf{e}}_z + r_m(\alpha, z, t)\hat{\mathbf{e}}_r\ . \tag{10}$$

The melt film coordinate system is defined as

$$\begin{aligned} \hat{\mathbf{e}}_\nu &= -\cos\alpha\hat{\mathbf{e}}_x - \sin\alpha\hat{\mathbf{e}}_y\ , \\ \hat{\mathbf{e}}_\alpha &= -\sin\alpha\hat{\mathbf{e}}_x + \cos\alpha\hat{\mathbf{e}}_y\ , \\ \hat{\mathbf{e}}_z &= \hat{\mathbf{e}}_z \end{aligned} \tag{11}$$

and a position $\mathbf{x}$ inside the liquid volume Ω_l as

$$\mathbf{x} = \mathbf{x}_m + \nu\hat{\mathbf{e}}_\nu\ . \tag{12}$$

Given the orthogonality of this coordinate system, the differential operators are expressed with the scaling factors

$$\begin{aligned} h_1 = h_\nu &= \left|\tfrac{\partial\mathbf{x}}{\partial\nu}\right| &&= 1\ , \\ h_2 = h_\alpha &= \left|\tfrac{\partial\mathbf{x}}{\partial\alpha}\right| &&= \sqrt{(\nu - r_m)^2 + (\partial_\alpha r_m)^2}\ , \\ h_3 = h_z &= \left|\tfrac{\partial\mathbf{x}}{\partial z}\right| &&= \sqrt{1 + (\partial_z r_m)^2}\ . \end{aligned} \tag{13}$$

2.4. Scaling for the liquid phase

The coordinates $\left\{\nu', \alpha', z'\right\}$ and the time t are scaled by typical quantities as coordinates $\{\nu, \alpha, z\}$ and time τ. The primed quantities denote unscaled quantities.

$$\nu' = t_m\nu,\ \alpha' = \alpha,\ z' = az,\ r' = w_0 r,\ t = \frac{t_m}{v_0}\tau \tag{14}$$

The scaled velocities $\mathbf{u} = \{u_\nu, u_\alpha, u_z\}$ are given by

$$v_\nu = v_0 u_\nu\ ,\ v_\alpha = \frac{w_0}{t_m} v_0 u_\alpha\ ,\quad v_z = \frac{a}{t_m} v_0 u_z\ . \tag{15}$$

and the scaling factors translate to

$$h_\nu = h'_\nu\ ,\ h_\alpha = w_0 h'_\alpha\ ,\ h_z = h'_z\ . \tag{16}$$

The typical temperature θ maps the temperature T to the interval between ambient temperature T_a and melting temperature T_m and the scaled pressure Π is given by

$$T = (T_m - T_a)\theta + T_a,\ p = \frac{a^2\,\varrho\,\nu_l v_0}{t_m^3}\Pi \tag{17}$$

The hierarchy of the spatial dimensions is reflected by the small parameters γ, δ and ϵ

$$\epsilon = \frac{t_m}{a} \ll \delta = \frac{t_m}{w_0} \quad \wedge \quad \epsilon \ll \gamma = \frac{w_0}{a}\ . \tag{18}$$

For an exemplary cutting task in stainless steel the scales are $t_m = 30\,\mu\text{m}$, $w_0 = 300\,\mu\text{m}$ and $a = 6\,\text{mm}$. With the Reynolds number $\text{Re} = v_0 a\,\nu_l^{-1} = 224$ follows:

$$\epsilon = 0.005\ ,\ \delta = 0.1\ ,\ \gamma = 0.05 \tag{19}$$

with the relations

$$\begin{aligned} &\epsilon = \gamma\delta\ ,\ \delta^2 = \epsilon\tfrac{\delta}{\gamma} = \mathcal{O}(\epsilon)\ ,\ \gamma^2 = \epsilon\tfrac{\gamma}{\delta} = \mathcal{O}(\epsilon)\ , \\ &\epsilon\text{Re} = \text{Re}^* = \mathcal{O}(1)\ . \end{aligned} \tag{20}$$

The derivatives of h_z with respect to α and z contain small parameters $\gamma^2 = \epsilon\gamma/\delta$

$$\begin{aligned} &\partial_\nu h_z = 0\ ,\ \partial_\alpha h_z = \gamma^2\tfrac{\partial_z r_m \partial_\alpha(\partial_z r_m)}{h_z}\ , \\ &\partial_z h_z = \gamma^2\tfrac{\partial_z r_m \partial_z^2 r_m}{h_z} \end{aligned} \tag{21}$$

and the derivative h_α with respect to ν contains the small parameter $\delta = \epsilon/\gamma$:

$$\partial_\nu h_\alpha = \epsilon\frac{1}{\gamma}\frac{\delta\nu - r_m}{h_\alpha} \tag{22}$$

2.5. Perturbation expansion

By transforming the Navier-Stokes equations (4) for mass balance, momentum balance and energy to conformal coordinates and by applying the scales denoted in Section 2.4, the resulting equations can be ordered by powers of the small parameter ϵ. The three equations for the scaled pressure Π, mass balance and energy balance show then the structure

$$\partial_\nu \Pi = \epsilon^2 f_{\nu 2} + \epsilon^3 f_{\nu 3} + \epsilon^4 f_{\nu 4} \,, \tag{23a}$$

$$\frac{1}{h_\alpha}\partial_\alpha \Pi = \epsilon^1 f_{\alpha 1} + \epsilon^2 f_{\alpha 2} + \epsilon^3 f_{\alpha 3} \,, \tag{23b}$$

$$\frac{1}{h_z}\partial_z \Pi = \epsilon^0 f_{z0} + \epsilon^1 f_{z1} + \epsilon^2 f_{z2} + \epsilon^3 f_{z3} \,, \tag{23c}$$

$$0 = \epsilon^0 f_{m0} + \epsilon^1 f_{m1} \,, \tag{23d}$$

$$0 = \epsilon^0 f_{\theta 0} + \epsilon^1 f_{\theta 1} + \epsilon^2 f_{\theta 2} + \epsilon^3 f_{\theta 3} \,. \tag{23e}$$

The functions $f_{\{\nu,\alpha,z,m,\theta\}}$ depend on the velocity components u_ν, u_α and u_z and their partial derivatives. For the leading order of ϵ these terms are:

$$\begin{aligned}
f_{\nu 2} &= -\mathrm{Re}^*\Big(\partial_\tau u_\nu + u_\nu \partial_\nu u_\nu + \tfrac{u_\alpha}{h_\alpha}\partial_\alpha u_\nu \\
&\quad + \tfrac{u_z}{h_z}\partial_z u_\nu - \tfrac{1}{\delta^2}\tfrac{u_\alpha^2}{h_\alpha}\partial_\nu h_\alpha\Big) - \tfrac{1}{h_\alpha h_z} \\
&\quad \cdot(\partial_z h_\alpha \partial_\nu u_z + h_\alpha \partial_\nu \partial_z u_z + h_z \partial_\alpha \partial_\nu u_\alpha) \\
f_{\alpha 1} &= \tfrac{\gamma}{\delta}\Big(\partial_\nu^2 u_\alpha + \mathrm{Re}^*\Big(\tfrac{1}{\gamma^2}\tfrac{u_z^2}{h_z h_\alpha}\partial_\alpha h_z \\
&\quad - \partial_\tau u_\alpha - \tfrac{1}{h_\alpha}u_\alpha \partial_\alpha u_\alpha - u_\nu \partial_\nu u_\alpha \\
&\quad - \tfrac{u_z u_\alpha}{h_z h_\alpha}\partial_z h_\alpha - \tfrac{u_z}{h_z}\partial_z u_\alpha\Big)\Big) \\
f_{z1} &= \partial_\nu^2 u_z - \mathrm{Re}^*\big(\partial_\tau u_z + \tfrac{1}{h_z}u_z \partial_z u_z \\
&\quad + \tfrac{1}{h_\alpha}u_\alpha \partial_\alpha u_z + u_\nu \partial_\nu u_z\big) \\
f_{m0} &= \partial_\nu u_\nu + \tfrac{1}{h_\alpha}\partial_\alpha u_\alpha + \tfrac{1}{h_z}\partial_z u_z \\
&\quad + \tfrac{1}{h_\alpha h_z}u_z \partial_z h_\alpha \\
f_{\theta 0} &= \tfrac{1}{h_\alpha}\partial_\nu^2 \theta
\end{aligned} \tag{24a}$$

The smallest order of each function f contains the time derivative of the matching $\mathbf{u}-$component. Halm [20] gave the full expressions for all terms in Eq. (23). The hierarchy of spatial dimensions is indicated by the leading ϵ-order of the momentum balance. $\mathcal{O}(\epsilon^0)$ is the leading order of the $z-$derivative of the pressure Π. The $\alpha-$derivative starts with $\mathcal{O}(\epsilon^1)$ and the $\nu-$derivative with $\mathcal{O}(\epsilon^2)$. This hierarchy enables a power series expansion of the solution quantities $\mathbf{u}$, Π and θ:

$$\begin{aligned}
\theta &= \theta_0 + \epsilon\theta_1 + \ldots + \epsilon^N \theta_N \\
\Pi &= \Pi_0 + \epsilon\Pi_1 + \ldots + \epsilon^N \Pi_N \\
\mathbf{u} &= \mathbf{u}_0 + \epsilon\mathbf{u}_1 + \ldots + \epsilon^N \mathbf{u}_N
\end{aligned} \tag{25}$$

By substituting Eq. (25) into Eq. (24) the solution can be determined iteratively. For the leading order $\mathcal{O}(\epsilon^0)$ follows

$$\begin{aligned}
\partial_\nu \Pi_0 = 0,\ \tfrac{1}{h_\alpha}\partial_\alpha \Pi_0 &= 0 \,, \\
\tfrac{1}{h_z}\partial_z \Pi_0 = f_{z0}(\mathbf{u}_0),\ 0 &= f_{m0}(\mathbf{u}_0)
\end{aligned} \tag{26}$$

and for the first order $\mathcal{O}(\epsilon^1)$

$$\begin{aligned}
&\partial_\nu \Pi_1 = 0,\ \tfrac{1}{h_\alpha}\partial_\alpha \Pi_1 = f_{\alpha 1}(\mathbf{u}_0) \,, \\
&\tfrac{1}{h_z}\partial_z \Pi_1 = f_{z0}(\mathbf{u}_1) + f_{z1}(\mathbf{u}_0) \,, \\
&0 = f_{\nabla 0}(\mathbf{u}_1) + f_{m1}(\mathbf{u}_0) \,.
\end{aligned} \tag{27}$$

The notation $f_{\{\nu,\alpha,z,m\}n}(\mathbf{u}_m)$ means that the $m-$th order of the power series expansion Eq. (25) is substituted into the $n-$th order of the perturbation series Eq. (24). Higher orders of ϵ can be solved analogical. The four equations for the leading order Eq. (26) have four unknowns and can be solved numerically. The energy equation is independent and can be solved subsequently. As long as all orders of ϵ are solved, the given formulation is exact. However, the leading order ϵ^0 already contains the essential solution characteristics and higher $\epsilon-$orders contribute as corrections only. For the analysis carried out in this paper, only the leading order is solved.

2.6. Integral model

A momentum method like presented by Kubota and Dewey [21] is used to reduce the problem size from 3*D* to 2*D*. A quadratic ansatz for the velocity profiles in azimuthal $\alpha-$ and axial $z-$direction is chosen. From Eq. (24d) follows a cubic ansatz for the radial $\nu-$direction and order $\mathcal{O}(\epsilon^0)$, so that

$$\begin{aligned}
u_{\nu 0} &= A_{\nu 0} + B_{\nu 0}\nu + C_{\nu 0}\nu^2 + D_{\nu 0}\nu^3 \,, \\
u_{\alpha 0} &= A_{\alpha 0} + B_{\alpha 0}\nu + C_{\alpha 0}\nu^2 \,, \\
u_{z0} &= A_{z0} + B_{z0}\nu + C_{z0}\nu^2 \,.
\end{aligned} \tag{28}$$

We define the integrated mass fluxes

$$m_\alpha = \int_0^h u_\alpha \mathrm{d}\nu \quad \text{and} \quad m_z = \int_0^h u_z \mathrm{d}\nu \,. \tag{29}$$

The coefficients in Eq. (28) can be derived from the boundary conditions. For the order $\mathcal{O}(\epsilon^0)$ the inflow $\mathbf{u}_m$ is applied at the melting boundary $\nu = 0$

$$u_{\{\nu,\alpha,z\}}\big|_{\nu=0} = u_{m\{\nu,\alpha,z\}}. \tag{30}$$

At the surface of the melt film $\nu = h$ the surface tension due to the process gas flow is applied

$$\partial_\nu u_\alpha|_{\nu=0} = \tau_\alpha,\ \ \partial_\nu u_z|_{\nu=0} = \tau_z \,, \tag{31}$$

so that the coefficients for $\alpha-$ and $z-$direction of the zero-th order can be determined as

$$\begin{aligned}
A_{\{\alpha,z\}0} &= u_{m\{\alpha,z\}} \,, \\
B_{\{\alpha,z\}0} &= \tfrac{3m_{\{\alpha,z\}0}}{h^2} - \tfrac{3u_{m\{\alpha,z\}}}{h} - \tfrac{\tau_{\{\alpha,z\}}}{2} \,, \\
C_{\{\alpha,z\}0} &= -\tfrac{3m_{\{\alpha,z\}0}}{2h^3} + \tfrac{3u_{m\{\alpha,z\}}}{2h^2} - \tfrac{3\tau_{\{\alpha,z\}}}{4h} \,.
\end{aligned} \tag{32}$$

By equating the coefficients $u_{\nu 0}$ is defined by

$$\begin{aligned}
A_{\nu 0} &= u_{m\nu} \,, \\
B_{\nu 0} &= -\Big(\tfrac{\partial_\alpha A_{\alpha 0}}{h_\alpha} + \tfrac{\partial_z h_\alpha A_{z0}}{h_\alpha h_z} + \tfrac{\partial_z A_{z0}}{h_z}\Big) \,, \\
C_{\nu 0} &= -\tfrac{1}{2}\Big(\tfrac{\partial_\alpha B_{\alpha 0}}{h_\alpha} + \tfrac{\partial_z h_\alpha B_{z0}}{h_\alpha h_z} + \tfrac{\partial_z B_{z0}}{h_z}\Big) \,, \\
D_{\nu 0} &= -\tfrac{1}{3}\Big(\tfrac{\partial_\alpha C_{\alpha 0}}{h_\alpha} + \tfrac{\partial_z h_\alpha C_{z0}}{h_\alpha h_z} + \tfrac{\partial_z C_{z0}}{h_z}\Big) \,.
\end{aligned} \tag{33}$$

2.6.1. Kinematic boundary condition

The kinematic boundary condition Eq. (9) translates to a partial differential equation for the scaled melt film thickness h

$$\partial_\tau h = u_\nu - \frac{u_\alpha}{h_\alpha}\partial_\alpha h - \frac{u_z}{h_z}\partial_z h \,. \tag{34}$$

2.6.2. External pressure

The scaled pressure Π at the surface of the melt $\nu = h$ equals the scaled assist gas pressure Π_g.

The structure of the perturbation expansion Eq. (24) and the power series Eq. (25) requires Π_g to be expanded as

$$\Pi_g = \Pi|_{\nu=h} = \Pi_{g0}(z) + \epsilon\Pi_{g1}(\alpha, z) \,. \tag{35}$$

This means that the zero-th order of Π_g reflects only the $z-$dependency of the assist gas pressure at the apex of the cutting front

$$\Pi_{g0}(z) = \Pi_g(\alpha = 0, z) \tag{36}$$

and the first order contains corrections in azimuthal direction

$$\Pi_{g1}(\alpha, z) = \frac{1}{\epsilon}(\Pi_g - \Pi_{g0}) \,. \tag{37}$$

2.7. Zero-th order model equations

By substituting Eq. (25) into Eq. (24) and integrating over ν the conditional equation for the quantities melt film thickness h and zero-th order mass fluxes $m_{\alpha 0}$ and m_{z0} can be obtained

$$\partial_\tau \mathbf{Q}_0 + \frac{1}{h_\alpha h_z}[\partial_\alpha (h_z \mathbf{F}_{\alpha 0}) + \partial_z (h_\alpha \mathbf{F}_{z0})] = \mathbf{S}_0 \,, \tag{38}$$

for the quantities

$$\mathbf{Q}_0 = (m_{\alpha 0}, m_{z0}, h)^T \,, \tag{39}$$

the convective zero-th order fluxes

$$\begin{aligned} \mathbf{F}_{\alpha 0} &= \left(\int_0^h u_{\alpha 0}^2 \mathrm{d}\nu, \int_0^h u_{\alpha 0} u_{z0} \mathrm{d}\nu, m_\alpha \right)^T \,, \\ \mathbf{F}_{z0} &= \left(\int_0^h u_{\alpha 0} u_{z0} \mathrm{d}\nu, \int_0^h u_{z0}^2 \mathrm{d}\nu, m_z \right)^T \,, \end{aligned} \tag{40}$$

and the source term

$$\mathbf{S}_0 = (S_{\alpha 0}, S_{z0}, S_h)^T \,, \tag{41}$$

with

$$\begin{aligned} S_{\alpha 0} &= -\frac{1}{\mathrm{Re}^*}\Big[\frac{1}{h_\alpha}\frac{\delta}{\gamma}\partial_\alpha \Pi_{g1} h + \frac{3 m_{\alpha 0}}{h^2} - \frac{3 u_{m\alpha}}{h} \\ &\quad - \frac{3\tau_\alpha}{2}\Big] + u_{m\alpha} u_{m\nu} + \frac{1}{\gamma^2}\frac{\partial_\alpha h_z}{h_\alpha h_z}\int_0^h u_{z0}^2 \mathrm{d}\nu \\ &\quad - \frac{\partial_z h_\alpha}{h_\alpha h_z}\int_0^h u_{\alpha 0} u_{z0} \mathrm{d}\nu \,, \\ S_{z0} &= -\frac{1}{\mathrm{Re}^*}\Big[\frac{1}{h_z}\partial_z \Pi_{g0} h + \frac{3 m_{z0}}{h^2} - \frac{3 u_{mz}}{h} \\ &\quad - \frac{3\tau_z}{2}\Big] - u_{m\nu} u_{mz} \,, \\ S_h &= u_{m\nu} - h_z \partial_\nu h_\alpha \int_0^h u_\nu \mathrm{d}\nu - m_\alpha \partial_\alpha h_z \,. \end{aligned} \tag{42}$$

Note:

- h_α contains the radial coordinate ν. To integrate these terms successfully, expression containing h_α have to be expanded at $\nu = 0$ and evaluated at $\nu = h$. Some derivatives of h_α contain the small parameter ϵ and can be assigned to higher orders and are removed from the zero-th order equations.
- h_α behaves very smooth and changes slowly across the melting surface, so this expansion does not create considerable errors.
- The source term for h Eq. (42) and the 3rd component of the flux Eq. (40) contain the full series expression for u_ν, m_α and m_z. So, if computing higher orders, these have to be considered in the equation for h.

2.8. Limit $h \to 0$

For vanishing melt film thicknesses $h \to 0$, the limiting behavior has to be considered. For $h < h_{\min}$ follows

$$\begin{aligned} h &= h_{\min} \,, \\ m_\alpha &= u_{m\alpha} h_{\min} + \tfrac{1}{2}\tau_\alpha h_{\min}^2 \,, \\ m_z &= u_{mz} h_{\min} + \tfrac{1}{2}\tau_z h_{\min}^2 \,. \end{aligned} \tag{43}$$

$h_{\min}$ is a model parameter and has to be adjusted so that the numeric provides stable solutions. In the presented work we set $h_{\min} = 0.01$ in scaled units.

2.9. Zero-th order energy equation

The small parameter expansion for the scaled temperature θ Eq. (24a) contains no time derivative. The structure of the perturbation expansion states that the essential solution for the temperature is linearly in $\nu-$direction and applies instantly

$$\theta_0 = A_{\theta 0} + B_{\theta 0}\nu \,. \tag{44}$$

The coefficients can be determined by the boundary conditions

$$\begin{aligned} \theta_0|_{\nu=0} &= A_{\theta 0} = 1 \,, \\ \partial_\nu \theta_0|_{\nu=h} &= B_{\theta 0} = q_a \sqrt{1 + \left(\tfrac{\partial_\alpha h}{h_\alpha}\right)^2 + \left(\tfrac{\partial_z h}{h_z}\right)^2} \,, \end{aligned} \tag{45}$$

where 1 equals the scaled melting temperature at the melting front and q_a the scaled heat flux applied by the laser beam at the melt film surface. Cooling effects due to evaporation, assist gas flow or thermal radiation are neglected in this stage of the model and should be added in future improvements.

2.10. Absorbed energy flux density

The absorption characteristics of focused laser light has to be taken into account to calculate the absorbed energy flux density q_a on the melt film surface. This absorption depends on the direction of the incident laser beam $\hat{\mathbf{S}}$ projected on the surface normal $\mathbf{n}$

$$\mu = -\hat{\mathbf{S}} \cdot \mathbf{n} \,, \tag{46}$$

the wavelength λ of the laser light and the absorbing material. For metallic materials the absorption A can be calculated using the high conductivity limit as presented by Bergström et al. [22]

$$\begin{aligned} A_s(\mu) &= \frac{4\epsilon_\lambda \mu}{2 + 2\epsilon_\lambda + \epsilon_\lambda^2 \mu^2} \,, \\ A_p(\mu) &= \frac{4\epsilon_\lambda \mu}{2\mu^2 + 2\epsilon_\lambda + \epsilon_\lambda^2} \,, \end{aligned} \tag{47}$$

for radiation with a plane of incidence that is perpendicular or parallel to the surface. ϵ_λ is a material parameter that depends on the wavelength and the material. Petring [23] measured this parameter for steel for fiber ($\lambda = 1.064\,\mu$m) and CO_2 lasers ($\lambda = 10.6\mu$m)

$$\begin{aligned} \epsilon_{1.064} &= 0.25 \,, \\ \epsilon_{10.6} &= 0.05 \,. \end{aligned} \tag{48}$$

The result for mixed polarization is shown in Fig. 8.

Arntz et al. [8] demonstrated, that multiple reflection show a considerable effect on the lower parts of the cut surface. To account this ray-tracing is performed inside the cutting kerf. The principle is shown in Fig. 7. The initial intensity distribution for the ray-tracer is retrieved from a Gaussian beam propagation of a given intensity profile as presented by Svelto [24]. As distribution we assume super-Gaussian beam distributions of order n to take varying beam profiles in the real process into account

$$f(\mathbf{x}) = \frac{\sqrt[n]{4}}{\Gamma\left(\frac{2+n}{n}\right)} \exp\left\{ -2\left(\frac{\sqrt{x^2 + y^2}}{w(z)} \right)^2 \right\} \,, \tag{49}$$

with the gamma function Γ and beam radius function along the optical axis z

$$w(z) = w_0 \sqrt{1 + \left(\frac{z - z_0}{z_R} \right)^2} \,, \tag{50}$$

for a given beam radius w_0 at focal point z_0 and Rayleigh length z_R. The direction of the Poynting vector $\hat{\mathbf{S}}$, which is required for the ray-tracing, is retrieved from the time-averaged phase-factor

$$\Phi = -\frac{2\pi z}{\lambda} - \frac{z}{z_R}\frac{x^2 + y^2}{w(z)^2} + \arctan\frac{z}{z_R} \tag{51}$$

as

$$\hat{\mathbf{S}}(\mathbf{x}) = \frac{\nabla \Phi(\mathbf{x})}{|\nabla \Phi(\mathbf{x})|} \,. \tag{52}$$

2.11. Motion of the melting front

The melting front Γ_i^m shown in Fig. 5 is a free moving boundary and its motion depends on the difference of the normal heat flux densities into the solid material q_s and the liquid material q_l

$$q_s = \mathbf{q}_s \cdot \mathbf{n} = (\nabla \theta) \cdot \mathbf{n}, \;\; q_l = \mathbf{q}_l \cdot \mathbf{n} \,. \tag{53}$$

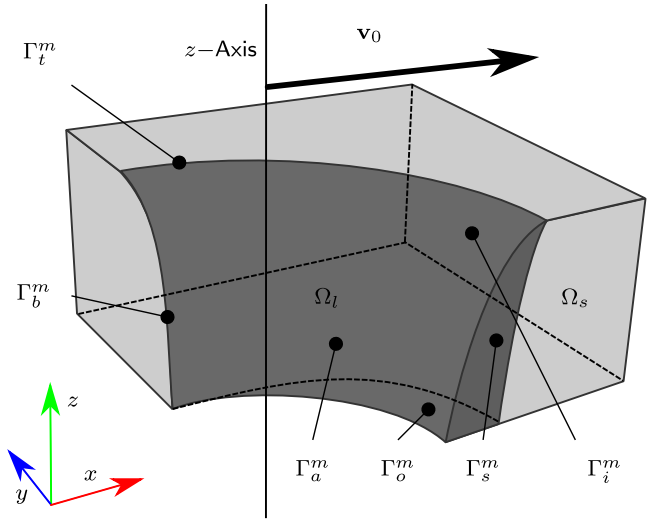

Fig. 5. Physical domains for the solid Ω_s and the liquid phase Ω_l. The liquid domain is bound by inflow Γ_i^m, outflow Γ_o^m, absorption Γ_a^m and symmetry Γ_s^m boundaries.

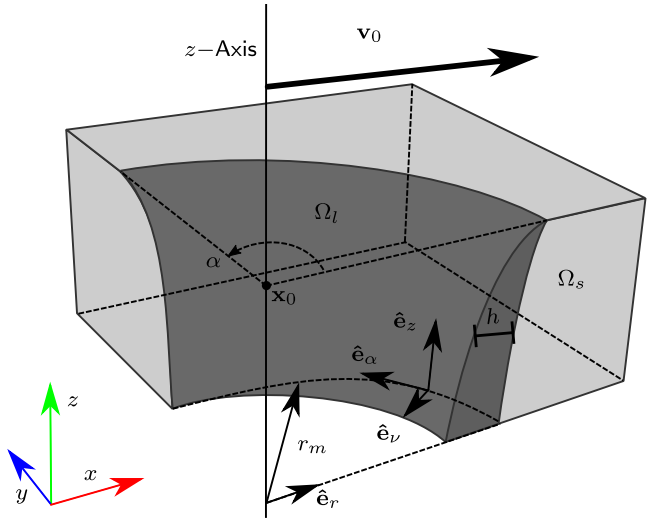

Fig. 6. Conformal coordinates $\{\nu, \alpha, z\}$ for the melt film in laser fusion cutting. The reference point is $\mathbf{x}_0 = (0, 0, 0)$.

The velocity of the melting front v_p is defined by a Stefan-Signorini problem (Friedman and Jiang [25])

$$v_p = \frac{1}{h_m}(q_l - q_s) \,. \tag{54}$$

To describe the motion of the melting front, it is transformed into cylindrical coordinates (r, α, z) and described by the distance function $\phi(\alpha, z)$. Its equation of motion

$$\partial_t \phi + \mathbf{v}\nabla\phi = 0 \tag{55}$$

is solved with a Hamilton-Jacobi formalism (Landau and Lifshitz [26]). The normal velocity for the distance function v_n is the sum of the normal velocity of the melting front and projected motion of the moving frame of reference $-v_0\hat{\mathbf{e}}_x$

$$v_n = v_p - v_0\hat{\mathbf{e}}_x \cdot \mathbf{n} \,. \tag{56}$$

The motion of the melting front mesh is illustrated in the video presented in Section 3.1. The additional motion of the part $-v_0\hat{\mathbf{e}}_x$ adds a challenge to the numerical representation of the melting front. Since only discrete radii are covered by the distance function, the very slow motion overlay blurs the structure of the recrystallized melting front and thus the simulation result for the striation pattern. The structure of the melting front is displayed in Fig. 9. To retain the fine structure of the melting front, the distance function ϕ is only evaluated, if the surface temperature is at melting temperature. For all other points of the melting front, which carry no melt film in the current time step, the motion of the part $-v_0\hat{\mathbf{e}}_x$ is applied directly to the distance function.

To ensure this mechanism works, the numerical resolution of the melting front is doubled in azimuthal and axial direction. Fig. 10 shows, that no significant difference in striation wavelength and amplitude shows up for the higher resolution.

2.12. Numerical simulation

The numerical simulation is implemented as in-house C++ code and is paralleled using the *OpenMP* paradigm where possible. Fig. 9 shows the computational mesh as conformal hexahedral mesh for the solid phase. The front part ($x \geq 0$) is structured as radial mesh around the $z-$axis. By placing the $z-$axis behind the laser beam axis the radial part of the mesh is large enough to simulate the molten zone. The surface mesh of the radial part is a structured quadrilateral mesh in 3*D* and used for the motion of the melting front and the simulation of the melt film equations Eq. (38). A virtual quadrilateral mesh with the same structure, but translated by the melt film thickness h in radial direction is used as input for the ray-tracer.

Inside the solid phase the heat equation is solved by a standard finite element method (FEM) using linear test functions. The melt film equations for the zero-th order are solved with a finite volume method (FVM) using explicit time stepping and the upwind difference scheme for calculation of the convective fluxes. To avoid numerical instabilities the time stepping of the liquid phase is separated from the global time stepping of the solid phase and the melting front. This allow the FVM solver to perform much smaller time steps than the global time step without slowing down the computation too much.

A resulting image of the numerical simulation is shown in Fig. 11. The fine-scaled striation pattern on the left cut surface is created from a record of the motion of the melting front and does not reflect the resolution of the solid phase, which is coarser in this region.

The numerical resolution for this simulation is $\Delta\alpha r \approx 25\,\mu$m, $\Delta z = 50\,\mu$m and $\Delta r \approx 20\,\mu$m in the area of the melting front. The hexahedral mesh for the solid phase consists of 346860 linear elements, the quadrilateral mesh of 3660 elements and the ray-tracing is done by 234240 incidenting rays. For a cut length of $L = 7.5$ mm, a cut thickness of $a = 3$ mm and a cutting speed of $v_0 = 1\,\mathrm{m\,min^{-1}}$ the solution time is around 12 h on a quad-Xeon-8168 system at 2.7 GHz. The radial extent of the calculation domain is 15 mm and the rear extent is 50 mm, so that the outer boundaries show no effect on the melting front.

3. Findings

To evaluate the model and solution structure of the proposed simulation, the experiments of Hirano and Fabbro [4] are analyzed for the parameters given as *Ref. II* in Tab. 1. The technically more relevant parameters for *Ref. I* cannot be simulated with this model because of the restrictions given under *Limitations* in the conclusion. The following cases are simulated:

- Variation of cutting speed for fiber laser.
- Variation of beam profile for fiber laser.
- Gaussian and tophat beam shape for fiber and CO_2 laser.

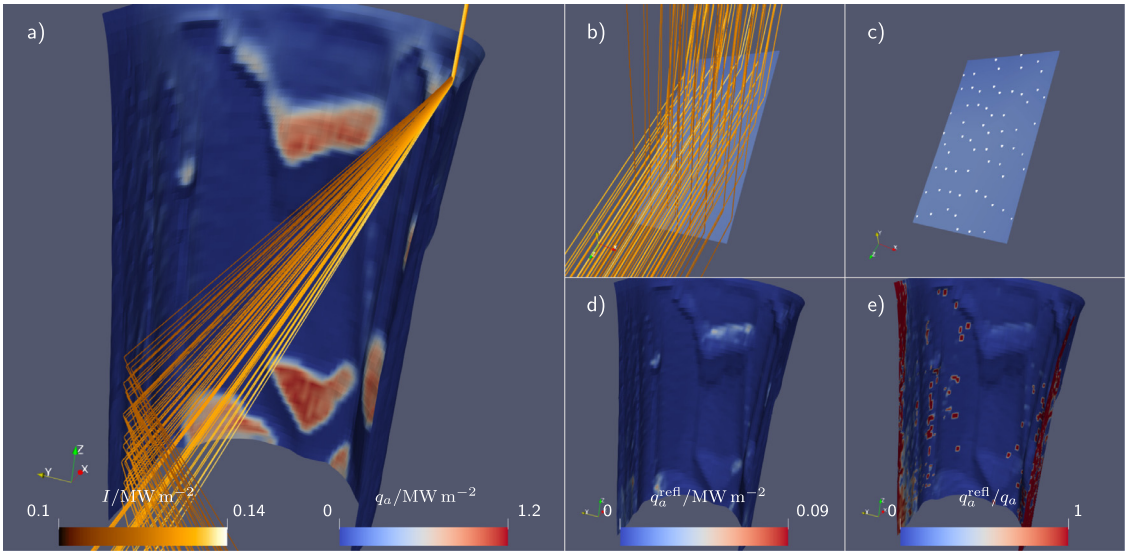

Fig. 7. a) Ray tracing inside the cutting kerf with ray batch reflected by a single surface element. b) Zoom of the reflecting surface element. c) Randomized source points for initial rays. d) Heat flux due to multiple reflections. e) Contribution of multiple reflections compared to direct absorption.

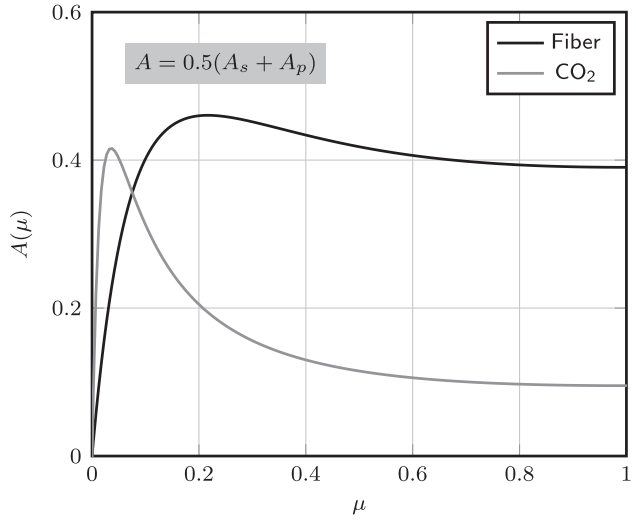

Fig. 8. Absorption for circular polarization depending on the cosine of the angle of incidence for fiber and CO_2 lasers on steel.

Table 2
Material parameters used for simulation.

Parameter	Symb./Unit	Value
Melting temperature	T_m/K	1712
Mass density	ϱ/kg m^{-3}	7545
Spec. heat cap.	c_p/J kg^{-1}K^{-1}	51
Heat conductivity	k/W m^{-1}K^{-1}	31
Kinematic viscosity	ν_l/m^{2}s^{-1}	8.9×10^{-7}
Heat of fusion	H_m/J Kg^{-1}	2.77×10^5

Tab. 2 gives the material parameters used, which are considered as constant in the simulation.

To classify the simulation results, comparisons with experimental results are drawn where possible.

3.1. Numerical solution results

Fig. 12 shows a video of the cutting simulation for the parameters *Ref. II* of Tab. 1. The upper part shows the thermal simula-

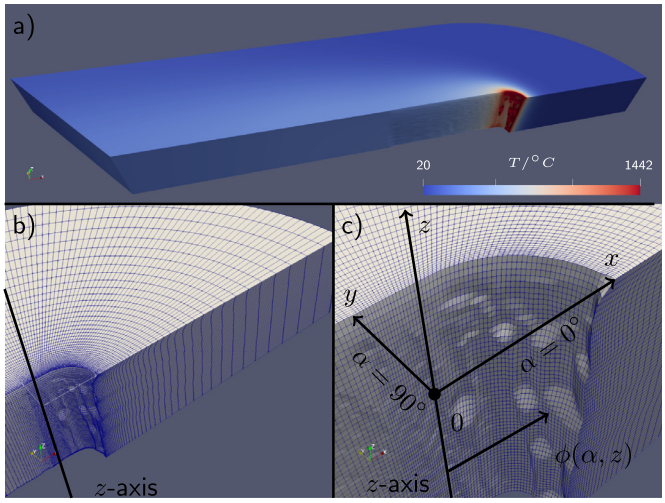

Fig. 9. a) Calculation domain of the solid phase. b) Structured computational mesh. c) Zoom of the melting front. The result of the distance function ϕ is used to deform the mesh during the simulation.

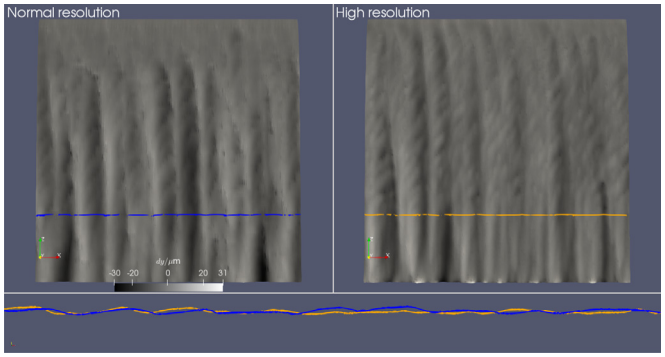

Fig. 10. Simulated striation patterns for default numerical resolution (left) and doubled resolution (right). The surface contour at 75% depth is extracted at the bottom to compare the striation wave length and amplitude. The quantity *dy* is the deviation from the horizontal mean value of the surface coordinate *y*.

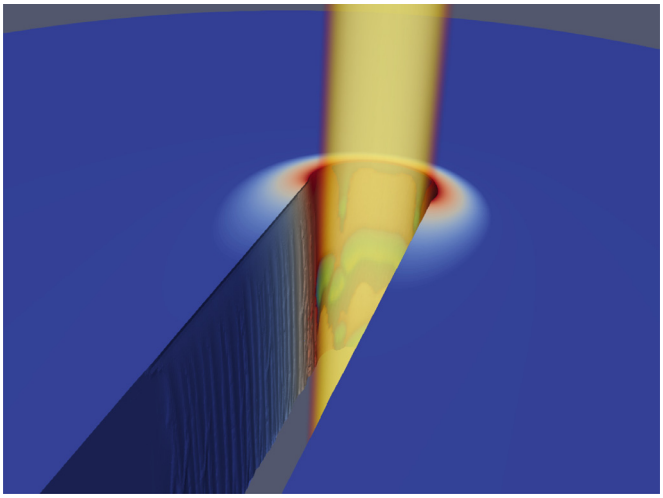

Fig. 11. Simulation of laser cutting. The calculated fine-scaled striation pattern is visible on the left cut surface.

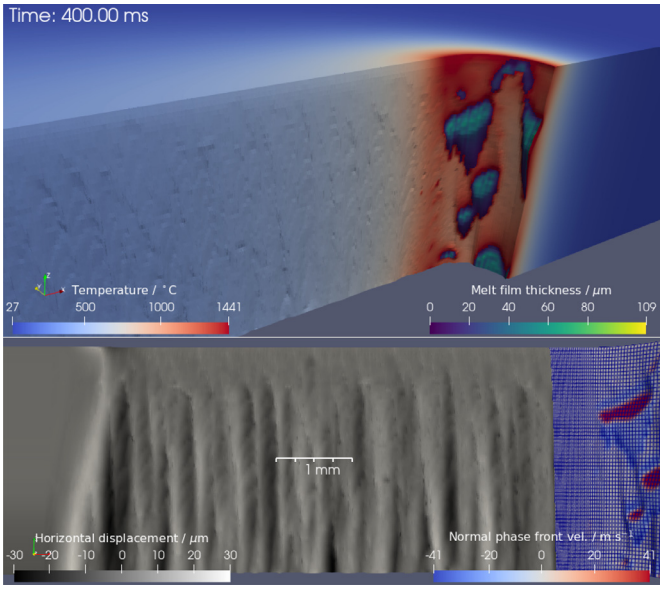

Fig. 12. Numerical simulation of laser fusion cutting. See final section "Supplementary material" for the supplied video file. sss=

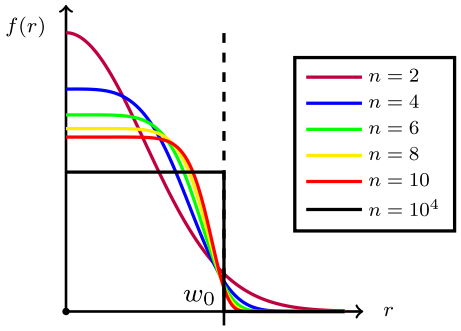

Fig. 13. Super-Gaussian beam profiles for several exponents n. $n = 2$ equals Gaussian distribution.

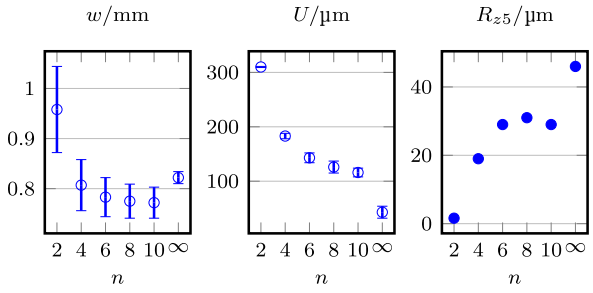

Fig. 14. Half kerf width w, angular tolerance U and mean profile height R_{z5} for different exponents n of a super-Gaussian beam distribution.

tion of the solid material in the coordinate system of the laser beam. For melt film thicknesses $h > h_{\min}$ the melt film is drawn as overlay on the solid material. On that parts of the melting front, where no melt film or a vanishing melt film thickness is present, the surface temperature can drop below the melting temperature. The removal of the melt happens in separated melt humps, that are driven by a parametrized assist gas flow. Formation of dross due to adherent melt droplets at the lower edge of the cut is not included in this model. Fast appearing temperature hot spots are caused by multiple reflections. The geometry is reflected on the symmetry plane for the raytracer. The geometry of the cut surface is overlain by a recording of the moving mesh, so that the displayed resolution of the cut surface is much higher than the actual resolution of the numerical mesh that is used for the thermal calculation.

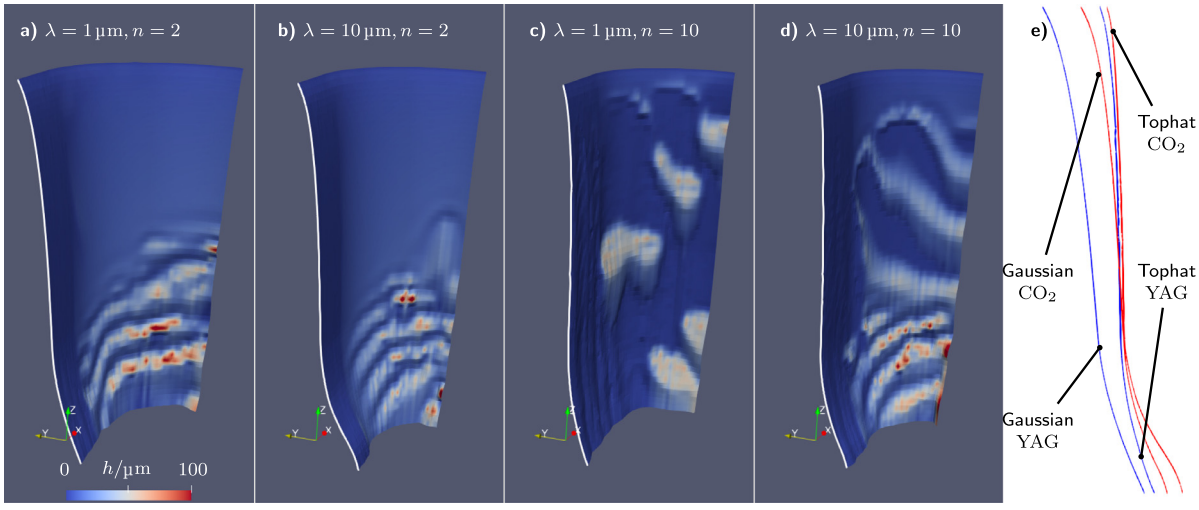

Fig. 15. Structure of melting front and melt waves for Gaussian ($n = 2$) and tophat ($n = 10$) beam shapes for fiber ($\lambda = 1\,\mu$m) and CO_2 ($\lambda = 10\,\mu$m) lasers.

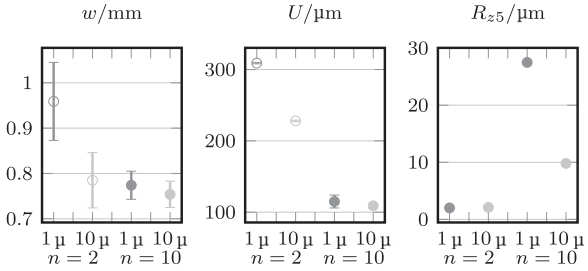

Fig. 16. Gaussian and Super-Gaussian beam profile.

Table 3
Mean profile height R_{z5}, striation wavelength λ_R and mean half kerf width w for experiments by Hirano and Fabbro [4] (E) and simulation (S).

$\frac{v_0}{\mathrm{m\ min^{-1}}}$	$\frac{R_{z5}}{\mu\mathrm{m}}$ (E)	$\frac{R_{z5}}{\mu\mathrm{m}}$ (S)	$\frac{\lambda_R}{\mu\mathrm{m}}$ (E)	$\frac{\lambda_R}{\mathrm{mm}}$ (S)	$\frac{w}{\mathrm{mm}}$ (E)	$\frac{w}{\mathrm{mm}}$ (S)
1	65	33	375	277	0.875	0.77
2	55	26	355	263	0.85	0.75
3	40	x	200	x	0.85	x
6	x	9	x	166	0.84	0.7

The melting front as front part of the cutting kerf and its numerical mesh is shown in the lower part of the video. The camera position is locked perpendicular to a fixed point on the cut surface, so that the melting front moves to the right. The parts of the melting front with a non-zero normal phase front velocity v_p (i.e. melting or recrystallizing) are colored in blue or red. For dry parts of the mesh, the cutting speed v_0 is directly transferred to the mesh as described in Section 2.11. The leftmost column of the melting front mesh defines the geometric transition to the cut surface and is recorded for each timestep to reconstruct a high-resolution image of the striation pattern. On the cut surface the deviation from the horizontal mean value of the lateral surface coordinate y is colored in gray-scale.

The recorded striation pattern is used for the evaluations presented in this paper.

3.2. Variation of cutting speed

For the parameters *Ref. II* of Tab. 1 the cutting speed is varied between $1\,\mathrm{m\,min^{-1}}$ and $6\,\mathrm{m\,min^{-1}}$ and mean profile height R_{z5}, striation wavelength λ_R and half kerf width w are compared to experimental results published by Hirano and Fabbro [4].

The result of the comparison is provided in Tab. 3. All three quantities decrease with increasing cutting speed v_0. This behavior is reflected correctly in the simulation. The mean profile height is underestimated by a factor of ≈ 0.5, the striation wavelength by ≈ 0.75 and the half width by ≈ 0.85. The relative deviation is nearly constant within each quantity, so the tendency is correctly reproduced by the simulation. Possible reasons for the deviation itself are given under *Limitations*.

Fig. 4 shows these tendencies for simulated half kerf widths w, angular tolerance U and mean profile height R_{z5}. All three tendencies match expectations from literature: The kerf width decreases with increasing cutting speed, the angular tolerance increases and the mean profile height decreases. This also points to a known optimization problem in laser fusion cutting: Simultaneous optimization of angular tolerance and mean profile height is hard to achieve.

3.3. Variation of beam profile

Another pair of contrary trends can be observed, when the beam profile is transmitted from plain Gaussian ($n = 2$) to a tophat profile ($n \to \infty$). Fig. 13 shows beam profiles for different orders n of the super-Gaussian distribution Eq. (49) for constant laser power P_L. The simulation results for half kerf width w, angular tolerance U and mean profile height R_{z5} are displayed in Fig. 14. The trend for the angular tolerance is clearly decreasing for increasing order of the super-Gaussian beam profile. This indicates that the steeper the beam distribution, the lower the angular tolerance which is desired in laser fusion cutting. The mean profile height behaves contrary and increases, if the beam profile becomes steeper. For a Gaussian beam profile the simulation calculates nearly zero mean profile height. This systematic underestimation of the mean profile height is explained at the section *Limitations*.

Table 4
Half kerf width w, angular tolerance U and mean profile height R_{z5} for different cutting speeds.

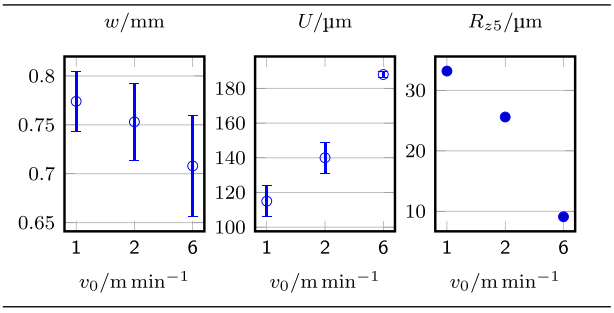

3.4. Variation of beam profile and wavelength

Another important issue in laser fusion cutting is the pronounced quality difference for fiber and CO_2 lasers. To demonstrate this difference kerf profiles for both types are simulated for Gaussian and tophat beam distributions. In practice CO_2 lasers operate with a nearly Gaussian beam shape and fiber lasers with a more tophat like beam shape. This corresponds to b) and c) of Fig. 15. This figure shows the melting front shape overlain with the melt film thickness h. The right hand side of each surface shows the apex of the melting front. The left hand side shows the outflow of the cut surface and its general profile indicated by a white line. The white line for each case is extracted at Fig. 16 e). It can be clearly seen, that tophat shapes ($n = 10$) show a steeper cut surface and a lower angular tolerance, compared to Gaussian beam shapes ($n = 2$). Moreover the CO_2 laser ($\lambda = 10\,\mu\mathrm{m}$) results in better angular tolerance. This is a direct result of the wavelength dependent absorption characteristics plotted in Fig. 8.

Another important finding of these simulations is the large qualitative difference in the structure of the melt waves. For Gaussian beam shapes and also for the tophat beam shape of the CO_2 laser noticeable melt waves form up that are connected over large parts of the cutting front. For a tophat beam shape and a fiber laser, the structure changes significantly to a more staircase-wise one with single, not interconnected steps. This indicates that one explanation for the significantly larger mean profile heights with fiber lasers can be found in the structural difference of how the melt is expelled from the cutting kerf.

Fig. 16 shows this difference in numbers. The fiber laser-tophat case produces a significantly larger mean profile height compared to the other cases. Again the plot shows, that an enhanced angular tolerance comes with a degradation of the mean profile height.

4. Conclusions

A reduced model for the simulation of the thin melt film in laser fusion cutting is presented that enables very fine spatial and

temporal resolution. To derive the model the governing equations are mapped to a conformal coordinate system and subjected to a scaling analysis. By expanding these equations into a perturbation series a hierarchy of spatial dimensions can be identified. The leading order of this expansion already reflects the essential characteristics of the full equations. Applying an integral approach the dimension can be reduced to $2D$, providing a huge advantage for computation. The numerical implementation of this zero-th order model already reproduces known trends in laser fusion cutting.

As essential result a contribution to the initial research questions can be made. The slope of the beam profile shows a direct effect to the angular tolerance and the mean profile height. The correlations are opposite, so an optimal design of a beam profile is a challenge for future research.

4.1. Limitations

For the initial step of the simulation, the zero-th order solution of the presented model equations, some strong assumptions have been made. The external pressure gradient and the driving forces are parameterized with a smooth behavior in axial and azimuthal directions. Local effects like evaporation and surface tension are neglected. This is the main reason, why the presented model is not able to calculate technically more relevant parameters like given in *Ref I.* of Tab. 1. To take these effects into account, corrections of the zero-th order, i.e. the $\mathcal{O}(\epsilon^1)$ order, have to be added to the solution to depict local effects like evaporation and surface tension. Both effects are required for stable cuts with smaller beam diameters and larger cut thicknesses.

Adding the next order of the model equations will have a huge impact on the numerical stability of the model. First tests show that more sophisticated numerical solution methods will be required for a stable simulation.

Another limitation is the assumption of temperature-independent material properties. Especially the dependency of the viscosity could have a strong impact on motion of the melt humps on the lateral part of the melting front. So-called momentum-source approaches should be added to the model to analyze the effect of increasing viscosity for decreasing temperature inside the melt.

Interaction with or a cooling effect by the assist gas flow and thermal radiation is neglected in this model.

4.2. Discussion

The presented model provides a new dimension of spatial and temporal resolution in simulation of melt film dynamics in laser fusion cutting. Cut lengths of several millimeters can be simulated with a resolution of several $10\,\mu$m on the whole cutting front withing reasonable computation times. The initial order of the model equations already reproduces known trends in laser fusion cutting and reveals a strong qualitative difference in the structure of the melt waves for fiber and CO_2 lasers. The presented model might be used to deepen the process understanding about the formation of striations in laser fusion cutting and to analyze and derive measures to enhance the quality of the cut surface.

4.3. Future work

To expand the region of applicability of the model higher order effects like surface tension and evaporation have to be taken into account. Solving the higher order terms will be a challenge for the numerical implementation. Temperature-dependencies should be considered in the material properties.

Funding

This research was funded by Deutsche Forschungsgemeinschaft (DFG) grand number (SFB1120).

Declaration of Competing Interest

The authors declare that they have no known competing financial interests or personal relationships that could have appeared to influence the work reported in this paper.

CRediT authorship contribution statement

U. Halm: Writing - original draft, Software, Investigation, Writing - review & editing. **M. Nießen:** Conceptualization, Methodology, Validation, Writing - review & editing. **W. Schulz:** Supervision, Writing - review & editing.

Acknowledgments

All presented investigations are conducted in the context of the Collaborative Research Center SFB1120 "Precision Melt Engineering" at RWTH Aachen University and funded by the German Research Foundation (DFG). For the sponsorship and support we wish to express our sincere gratitude.

Supplementary material

Supplementary material associated with this article can be found, in the online version, at 10.1016/j.ijheatmasstransfer.2020.120837

References

[1] Thermal cutting – Classification of thermal cuts – Geometrical product specification and quality tolerancesStandard, International Organization for Standardization, Geneva, CH, 2017.
[2] L.I. Green, G.L. Herrit, H.E. Reedy, New method for in-line beam profiling high-power co2 lasers with an ir camera-based system, Proc.SPIE 4969 (2003) 97–104, doi:10.1117/12.478986.
[3] W.-I. Cho, S.-J. Na, C. Thomy, F. Vollertsen, Numerical simulation of molten pool dynamics in high power disk laser welding, J. Mater. Process. Technol. 212 (1) (2012) 262–275, doi:10.1016/j.jmatprotec.2011.09.011.
[4] K. Hirano, R. Fabbro, Experimental investigation of hydrodynamics of melt layer during laser cutting of steel, J. Phys. D Appl. Phys. 44 (10) (2011) 105502, doi:10.1088/0022-3727/44/10/105502.
[5] S. Stelzer, A. Mahrle, A. Wetzig, E. Beyer, Experimental investigations on fusion cutting stainless steel with fiber and co2 laser beams, Physics Procedia 41 (2013) 399–404, doi:10.1016/j.phpro.2013.03.093. Lasers in Manufacturing (LiM 2013)
[6] K. Hirano, R. Fabbro, Possible explanations for different surface quality in laser cutting with 1 and 10 ôm beams, J. Laser Appl. 24 (1) (2012) 012006, doi:10.2351/1.3672477.
[7] E.H. Amara, K. Kheloufi, T. Tamsaout, R. Fabbro, K. Hirano, Numerical investigations on high-power laser cutting of metals, Appl. Phys. A 119 (4) (2015) 1245–1260, doi:10.1007/s00339-015-9154-8.
[8] D. Arntz, D. Petring, S. Stoyanov, U. Jansen, F. Schneider, R. Poprawe, In situ visualization of multiple reflections on the cut flank during laser cutting with 1ôm wavelength, J. Laser Appl. 30 (3) (2018) 032206, doi:10.2351/1.5040614.
[9] A.V. Zaitsev, G.V. Ermolaev, T.A. Polyanskiy, A.M. Gurin, Numerical simulation of the shape of laser cut for fiber and co2 lasers, AIP Conf. Proc. 1893 (1) (2017) 030046, doi:10.1063/1.5007504.
[10] A. Otto, M. Schmidt, Towards a universal numerical simulation model for laser material processing, Physics Procedia 5 (2010) 35–46, doi:10.1016/j.phpro.2010.08.120. Laser Assisted Net Shape Engineering 6, Proceedings of the LANE 2010
[11] S. Kohl, M. Schmidt, Numerical analysis of the influence of beam characteristics onto the process dynamics during laser cutting, International Congress on Applications of Lasers & Electro-Optics 2013 (1) (2013) 104–109, doi:10.2351/1.5062857.
[12] J. Zhao, P. Cheng, A lattice boltzmann method for simulating laser cutting of thin metal plates, Int. J. Heat Mass Transf. 110 (2017) 94–103, doi:10.1016/j.ijheatmasstransfer.2017.02.091.
[13] W. Schulz, V. Kostrykin, H. Zefferer, D. Petring, R. Poprawe, A free boundary problem related to laser beam fusion cutting: ode approximation, Int. J Heat Mass Transf. 40 (12) (1997) 2913–2928, doi:10.1016/S0017-9310(96)00342-0.

[14] W. Schulz, V. Kostrykin, M. Nießen, J. Michel, D. Petring, E.W. Kreutz, R. Poprawe, Dynamics of ripple formation and melt flow in laser beam cutting, J. Phys. D Appl. Phys. 32 (11) (1999) 1219, doi:10.1088/0022-3727/32/11/307.
[15] G. Vossen, J. Schüttler, Mathematical modelling and stability analysis for laser cutting, Math. Comput. Model Dyn. Syst. 18 (4) (2012) 439–463, doi:10.1080/13873954.2011.642387.
[16] W. Schulz, M. Nießen, U. Eppelt, K. Kowalick, Simulation of Laser Cutting, Springer Netherlands, Dordrecht, pp. 21–69. 10.1007/978-1-4020-9340-1
[17] U. Jansen, M. Niessen, W. Schulz, T. Hermanns, D. Arntz, R. Poprawe, Boundary layer approximation for melt film dynamics in laser fusion cutting, in: 22nd International Congress on Modelling and Simulation, 2017, pp. 326–332, doi:10.36334/modsim.2017.C1.Jansen. Hobart, Tasmania, Australia
[18] E. Lopez-Sandoval, A. Mello, Series solution of non linear partial differential equations from physical mathematical, CoRR abs/1206.2346 (2012).
[19] A. Mahrle, E. Beyer, Theoretical aspects of fibre laser cutting, J. Phys. D Appl. Phys. 42 (17) (2009) 175507, doi:10.1088/0022-3727/42/17/175507.
[20] U. Halm, Simulation hochdynamischer Vorgnge in der Schmelze beim Laserstrahlschneiden, RWTH Aachen University, 2018 Doctoral dissertation. ISBN: 978-3-8439-3884-6
[21] T. Kubota, C.F. Dewey, Momentum integral methods for the laminar free shear layer, AIAA Journal 2 (4) (1964) 625–629, doi:10.2514/3.2398.
[22] D. Bergström, A. Kaplan, J. Powell, Mathematical modelling of laser absorption mechanisms in metals: a review, M4PL16 workshop, Igls, Austria (2003).
[23] D. Petring, Anwendungsorientierte Modellierung des Laserstrahlschneidens zur rechnergestõtzten ProzeÛoptimierung, RWTH Aachen University, 1995 Doctoral dissertation. ISBN: 382650433X
[24] O. Svelto, Ray and Wave Propagation Through Optical Media, Springer US, Boston, MA, pp. 131–161. 10.1007/978-1-4419-1302-9
[25] A. Friedman, L.-S. Jiang, A stefan-signorini problem, J. Differ. Equ. 51 (2) (1984) 213–231, doi:10.1016/0022-0396(84)90108-6.
[26] L.D. Landau, E.M. Lifshitz, Mechanics, 3, Butterworth-Heinemann, 1976.